Microscopic flow near the surface of two-dimensional porous media. Part 1. Axial flow

By R. E. LARSON and J. J. L. HIGDON

Department of Chemical Engineering, University of Illinois,
1209 W California St, Urbana, Illinois 61801

A model problem is analysed to study the microscopic flow near the surface of two-dimensional porous media. In the idealized problem we consider axial flow through infinite and semi-infinite lattices of cylindrical inclusions. The effect of lattice geometry and inclusion shape on the permeability and surface flow are examined. Calculations show that the definition of a slip coefficient for a porous medium is meaningful only for extremely dilute systems. Brinkman's equation gives reasonable predictions for the rate of decay of the mean velocity for certain simple geometries, but fails for to predict the correct behaviour for media anisotropic in the plane normal to the flow direction.

1. Introduction

The flow of viscous fluid through permeable materials has been a problem of long-standing interest for fluid dynamicists. Historically, the study of such flows begins with Darcy's law (1856)

$$\boldsymbol{u} = -\frac{k}{\mu}\boldsymbol{\nabla}p.$$

This states that the average fluid velocity is proportional to the average pressure gradient. The coefficient k is a physical property of the porous material and has units of length squared. Although Darcy's law was originally proposed on empirical grounds, it may be justified theoretically for statistically homogeneous, isotropic materials and low-Reynolds-number fluid flow. For anisotropic media, the equation is easily generalized through the introduction of a permeability tensor $\boldsymbol{K}$

$$\boldsymbol{u} = -\frac{1}{\mu}\boldsymbol{K}\boldsymbol{\nabla}p.$$

Darcy's law has been applied to a vast array of problems involving flow through porous media and has proved to be a reliable model for flow in the interior of such materials.

Despite its success for interior flows, Darcy's law is not a complete model for porous media. When a fluid flows past a porous body of finite size, the interior flow must be matched with the exterior pure fluid flow at the boundary surface. Under normal circumstances, we require continuity of velocity and surface stress across this boundary; however, this is not possible owing to the reduced order of Darcy's law as compared with the Stokes equations. To circumvent this difficulty, one of two approaches is commonly employed. Beavers & Joseph (1967) proposed that Darcy's

law be retained for the interior flow, but that the boundary conditions be modified to match the exterior flow. They suggested a 'slip condition' of the form

$$\frac{\partial u}{\partial y}\bigg|_{y=0^+} = \frac{\alpha}{k^{\frac{1}{2}}}(u - u_{\mathrm{D}}).$$

Here u is the local average tangential velocity outside the body, u_{D} is the tangential velocity given by Darcy's law and α is the slip coefficient, a dimensionless constant depending on the local geometry of the interstices. The additional boundary conditions are continuity of normal velocity and normal stress. The slip condition was proposed on heuristic grounds to replace the smooth change in the flow field with a simple step change across a nominal boundary surface. Saffman (1971) gave theoretical justification for the slip condition of Beavers & Joseph and showed that the condition could be derived in the form

$$u = \frac{k^{\frac{1}{2}}}{\alpha}\frac{\partial u}{\partial y}\bigg|_{y=0^+} + O(k).$$

This expression is sufficient to calculate the outer flow correct to $O(k^{\frac{1}{2}})$. Saffman notes that detailed analysis of the transition region and precise definition of the nominal boundary ($y = 0$) are necessary to describe the slip velocity to higher order in k. In addition, the precise location of the nominal boundary surface will affect the value of the slip coefficient, even to the point that it may take on negative values.

A second approach to the problem of matching the interior and exterior flows is to replace Darcy's law with an equation of higher order. Brinkman (1947) proposed an extension of Darcy's law to describe flow near the surface

$$-\nabla p + \mu^* \nabla^2 u - \frac{\mu}{k} u = 0.$$

The first two terms represent the divergence of the local average viscous stress tensor incorporating an effective viscosity μ^*, while the third term represents the distributed resistance of the solid inclusions.

Because Brinkman's equation is of the same order as the Stokes equations, the standard continuity boundary conditions on velocity and stress may be applied. Howells (1974) used Brinkman's equation to calculate the drag on an impermeable particle immersed in an isotropic porous medium comprised of a random fixed array of particles and gave justification for setting μ^* equal to μ in the first approximation. For fixed arrays that are not sparse Brinkman originally suggested that the effective viscosity could account for the finite size of the inclusions.

Saffman (1971) examined the applicability of Brinkman's equation to the flow near the surface of a porous domain using averaged equations and gave as a more general result

$$\mu \int R_{ij}(x - \xi) u_j(\xi)\, \mathrm{d}\xi = \mu \nabla^2 u_i - \frac{\partial p}{\partial x_i}.$$

The integral on the left represent the distributed resistance of the averaged domain, evaluated at the point x. Each point ξ contributes a resistance proportional to the local average velocity and a resistance kernel dependent on both ξ and x. Brinkman's equation results when the distributed resistance is replaced by the simple Darcy term. This is achieved by approximating the resistance kernel with

$$R_{ij}(x - \xi) = \frac{\delta_{ij}}{k^\infty}\delta(x - \xi).$$

The corresponding resistance term for an anisotropic medium is

$$R_{ij}(x-\xi) = R_{ij}^{\infty}\,\delta(x-\xi),$$

and the resulting Brinkman equation is

$$-\nabla p + \mu\nabla^2 u - \mu\mathbf{R}u = 0.$$

The simple delta-function resistance kernels hold strictly for points in the interior of the porous medium, well away from the surface. More generally, we may expand the kernel as a series in the delta function and its derivatives, which would through integration lead to terms involving derivatives of u and resistance terms which vary with x across the porous boundary layer. Saffman concluded that the Darcy term for the resistance is not a useful approximation in this case. Unless further justification is given, the first and second derivatives of u should appear in the distributed resistance in order for the second derivatives in the div σ terms to be meaningful. Thus Brinkman's equation may not be a consistent approximation in the boundary region of interest, and the distinction between the effective viscosity and the fluid viscosity is not sufficient to resolve this difficulty.

Experimental studies to assess the usefulness of Brinkman's equation and slip conditions have been very limited. Beavers & Joseph (1967) conducted experiments on a rectangular channel with a porous wall. By measuring the increased flow rate compared with impermeable walls, they were able to calculate slip coefficients for two natural porous materials. Values of α from 0.1 to 4 were found and a strong dependence on geometric parameters other than the permeability was suspected. This view was confirmed by Beavers, Sparrow & Masha (1974), who found that the value of α for a certain material doubled after its surface was remachined. Taylor (1971) performed similar experiments with a grooved plate as a well-characterized model for an idealized porous medium. He found values of α ranging from 1.308 to > 7 as the thickness of the grooves was changed. Moreover, the experimental results showed good agreement with theoretical calculations for the same geometry by Richardson (1971). The relative utility of Brinkman's equation may be inferred from the above results by noting that continuity of stress and velocity is equivalent to assuming $\alpha = 1$ for these simple flows. In another study, Matsumoto & Suganuma (1977) measured the settling velocity of model flocs of steel wool and found good agreement with the velocities predicted by Brinkman's equation.

In the present effort we examine the microscopic flow in geometries representative of real porous media. We consider a variety of different media composed of periodic lattices of solid inclusions. Previous studies of periodic lattices have considered simple arrays of cylinders or spheres. Thus Sparrow & Loeffler (1959) studied axial flow through arrays of cylinders, while Sangani & Acrivos (1982*a*) analysed transverse flow in the same geometry. Zick & Homsy (1982) and Sangani & Acrivos (1982*b*) considered flow through cubic lattices of spheres. In all these efforts the goal was to find the permeability for infinite media. No attempt was made to consider flow over semi-infinite media or the effect of inclusion shape on the permeability. The primary goal of the present study is to address these issues by providing a precise description of the flow near the surface of porous media and evaluating the validity of the various macroscopic models. We shall restrict our attention to two-dimensional media, with the analysis and results for axial flow in this paper and the discussion of transverse flow in Part 2.

2. Mathematical formulation

We shall consider two model problems corresponding to flow in the interior and to flow near the surface of a two-dimensional porous medium. In the first problem the fluid flows axially through a doubly periodic lattice of cylinders under the action of a pressure gradient $dp/dz = -G$. In the second the lattice is semi-infinite in the y-direction, with a simple shear flow above the medium driving the flow in the surface layer. In this case the pressure gradient is zero, since the development of a pressure gradient would require a bounding surface above the pure fluid. The model geometry and coordinate system are sketched in figure 1.

With the assumption of unidirectional motion, the Navier–Stokes equations reduce to a simple Poisson equation for the axial velocity

$$\nabla^2 U = \frac{G}{\mu}. \tag{1}$$

The continuity equation guarantees that U and hence G are independent of z, while the absence of lateral flow implies that G is a constant. It is most convenient to separate U into a particular solution u_p satisfying (1) and a homogeneous solution u satisfying the two-dimensional Laplace equation $\nabla^2 u = 0$. For simplicity, u_p may be taken as any suitable quadratic function of x and y. Thus we are left to find the solution of Laplace's equation subject to boundary conditions of no slip on the solid surfaces and periodicity- or continuity-type conditions on the periodic cell boundaries. A more precise specification of the boundary conditions will be given below.

Since no analytical solutions are available for the complicated geometries under consideration, we must select an appropriate numerical technique. We have chosen the boundary-integral method, because it is easily adapted to different geometries and allows the straightforward implementation of periodic boundary conditions. In addition, it proves to be very well suited for an iterative solution of the semi-infinite problem.

Briefly, we start with the well-known Green identity for harmonic functions

$$u(\boldsymbol{x}_0) = \frac{1}{2\pi} \int_S \left[u(\boldsymbol{x}) \frac{\boldsymbol{r} \cdot \boldsymbol{n}}{r^2} - \log r \frac{\partial u}{\partial n}(\boldsymbol{x}) \right] dS, \quad (\boldsymbol{r} = \boldsymbol{x}_0 - \boldsymbol{x}), \tag{2}$$

which gives the value of a function at an interior point in terms of the values of the function and its normal derivative around the boundary of the domain (see e.g. Sneddon 1957, p. 194). For a point $\boldsymbol{x}_0$ on the boundary the well-known jump condition gives the same result except for a factor of 2:

$$u(\boldsymbol{x}_0) = \frac{1}{\pi} \int_S \left[u(\boldsymbol{x}) \frac{\boldsymbol{r} \cdot \boldsymbol{n}}{r^2} - \log r \frac{\partial u}{\partial n}(\boldsymbol{x}) \right] dS. \tag{3}$$

The specification of the boundary data for u or du/dn yields a Fredholm integral equation for the remaining function values. In the boundary-integral method the boundary shape and the functions u and du/dn are discretized in an appropriate manner, reducing the integral equation to a system of linear algebraic equations of the form

$$u(x_m) = \sum_n A_{mn} u(x_n) + \sum_n B_{mn} \frac{\partial u}{\partial n}(x_n). \tag{4}$$

Here $u(x_m)$ and $du/dn(x_m)$ represent function values at discrete points along the boundary, while the matrices A and B represent integrals along the discrete elements
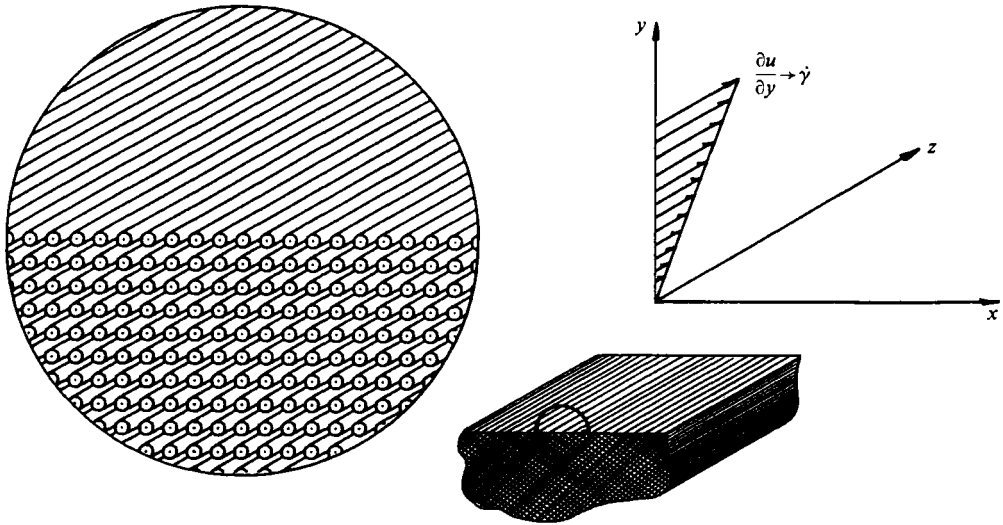
FIGURE 1. Model geometry for flow over the surface of a bounded porous medium.

making up the boundary. The exact form of A and B depends upon the specific discretization employed. A comprehensive discussion of various implementations may be found in the recent monograph edited by Brebbia (1983). In the present circumstances we choose the simplest representation with straight-line segments along the boundary and assume constant function values along each segment. This method is easy to apply and has the additional advantage that all integrations may be performed analytically, eliminating the need for special quadratures to deal with the singular kernels in (3). For smooth boundaries with continuous tangent vectors, this method gives errors $O(\delta^2)$, where δ is the length of a boundary segment. For piecewise-smooth boundaries with corners (such as encountered in our lattice cells) the error is $O(\delta^2)$ away from the corners, but $O(1)$ on the segment adjacent to the corner. This error arises from the $\boldsymbol{x} \cdot \boldsymbol{n}/r^2$ kernel and is proportional to du/ds, the derivative of u along the boundary. There are two ways to deal with this error. The first is to choose a particular solution such that du/ds is zero at the corner, eliminating the error entirely; the second is to choose variable length segments with progressively smaller segments near the corners. In either case the corner segment has negligible effect on the overall solution, and errors on other segments decrease as δ^2. A numerical test demonstrating the δ^2 error behaviour is shown in figure 2. All calculations presented in this paper were run on a CYBER 175 computer to a relative accuracy of at least 0.1 %.

The boundary-integral method gives the values of the functions u and du/dn at all points on the boundary. For many problems this is all the information required. In the present case, however, we need the total volume flow rate through the interstitial spaces to calculate the permeability of the lattice. Using Green's theorem

$$\int_V [u\nabla^2 v - v\nabla^2 u]\, dV = \oint_S \left[u\frac{\partial v}{\partial n} - v\frac{\partial u}{\partial n} \right] dS, \tag{5}$$

with u the axial velocity and $v = \frac{1}{4}r^2$ (or any function with $\nabla^2 v = 1$) yields

$$\int_V u\, dV = \oint_S \left[u(\tfrac{1}{2}\boldsymbol{r} \cdot \boldsymbol{n}) - \tfrac{1}{4}r^2 \frac{\partial u}{\partial n} \right] dS. \tag{6}$$
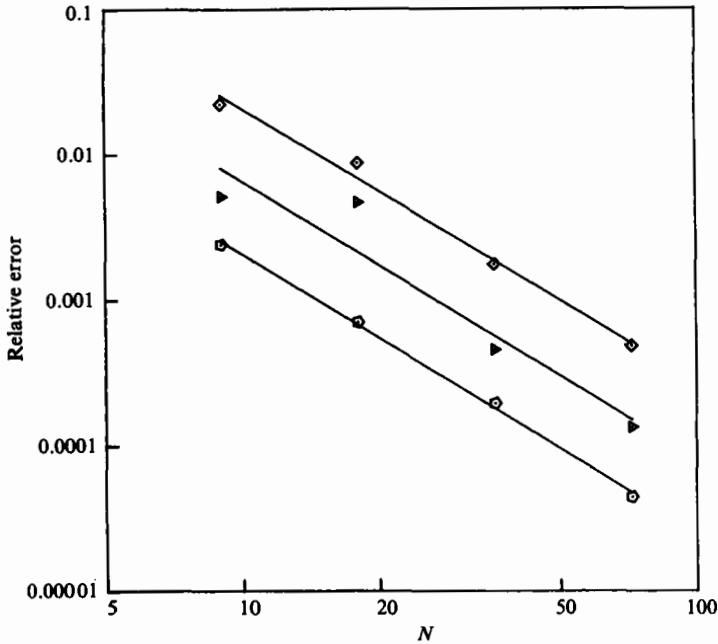
FIGURE 2. Relative error for permeability as a function of the number of discretization points in the boundary-integral method: $\diamondsuit$, $c = 0.7$; $\odot$, 0.1; $\triangledown$, 0.01.

Thus we may evaluate the total flow rate in terms of the calculated boundary values. Of course in our two-dimensional case the 'volume' integral is an area integral, and the 'surface' integral is around the perimeter of this domain. The flow rate due to the particular solution u_p may be evaluated with little effort by using numerical quadratures for the area integration.

2.1. Boundary conditions for infinite arrays

Consider a square lattice of circular cylinders, the simplest case among infinite arrays. The unit cell and coordinate system is shown in figure 3 (a). The dashed lines indicate the four symmetry axes for this configuration. For pressure-driven flow we choose a particular solution $u_p = \frac{1}{4}(G/\mu)(r^2 - a^2)$, where a is the cylinder radius. This choice preserves the problem symmetry and eliminates certain integrations. The no-slip condition requires $U = u_p + u = 0$ on the solid surface. Since $u_p = 0$ on this surface, we have the boundary condition $u = 0$ on the cylinder. On the fluid–fluid interface around the perimeter of the cell the combination of symmetry and periodicity requires that $dU/dn = 0$. Thus we have $du/dn = -du_p/dn$ on all fluid boundaries. This completes the specification of the boundary conditions for this lattice. Dividing the boundary into N discrete segments leaves N unknowns – the values of u on the fluid segments and the values of du/dn on the solid. These values are obtained from the solution of the linear system (4) by Gaussian elimination. In practice, we may exploit the eightfold symmetry to reduce the number of equations and unknowns to $\frac{1}{8}N$.

A more general two-dimensional array is shown in figure 3 (b). The solid boundary surface is labelled s while the two halves of the fluid boundary are labelled f_1 and f_2. Segments along f_1 are related to segments along f_2 by translations corresponding to basis vectors of the lattice. It might appear that the dashed parallelogram in figure

(a)

(b)
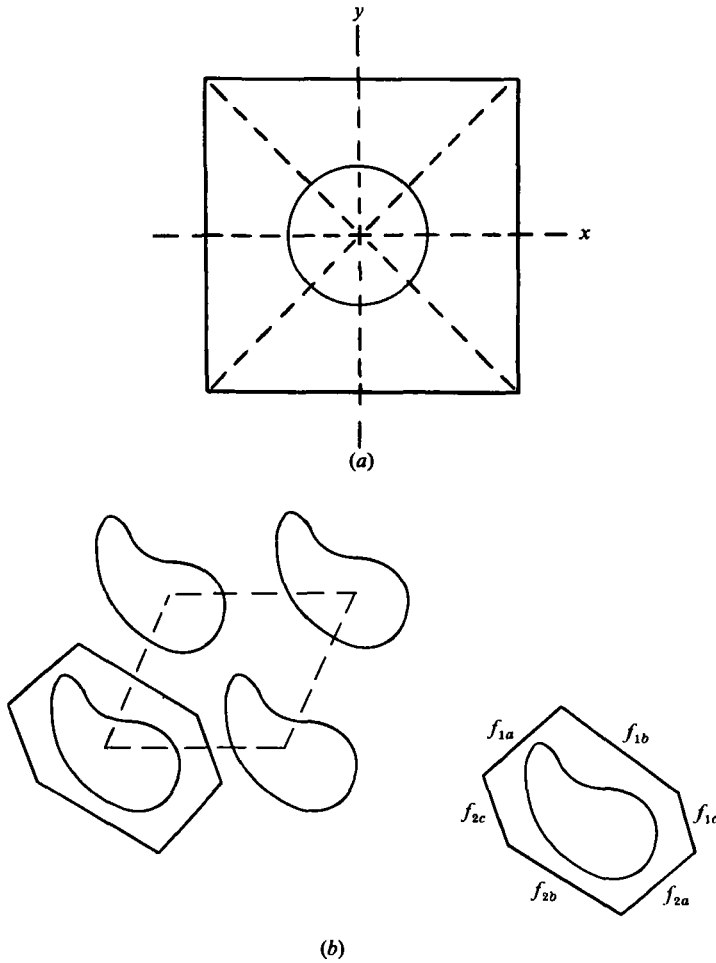
FIGURE 3. (a) Unit cell for an infinite square lattice of circular cylinders. Dashed lines represent symmetry planes. (b) Unit cell for a general lattice with arbitrary inclusion shape.

$3(b)$ would provide a simpler unit cell; however, the all-fluid cell boundary will prove more convenient when we consider semi-infinite arrays.

The no-slip condition for this array is $u = -u_p$ on surface s. The periodicity conditions on the cell perimeter are $(u)_{f_1} = (u)_{f_2}$ and $(du/dn)_{f_1} = -(du/dn)_{f_2}$, the minus sign arising owing to the change in the sense of the normal vector. Dividing the boundary into N segments again yields N unknowns – the values of du/dn on the solid and the values of u and du/dn on the fluid boundary f_1. The solution of the linear system (4) gives these values.

2.2. *Boundary conditions for semi-infinite arrays*

For semi-infinite lattices the flow field is periodic in the x-direction but extends from $-\infty$ to $+\infty$ in the y-direction. As shown in figure $4(a)$ for a simple square lattice, the domain covers a large number of cells both above and below the interface. If boundary conditions were specified on each cell independently, the problem would simply require the solution for each cell successively. Unfortunately, this is not the case.
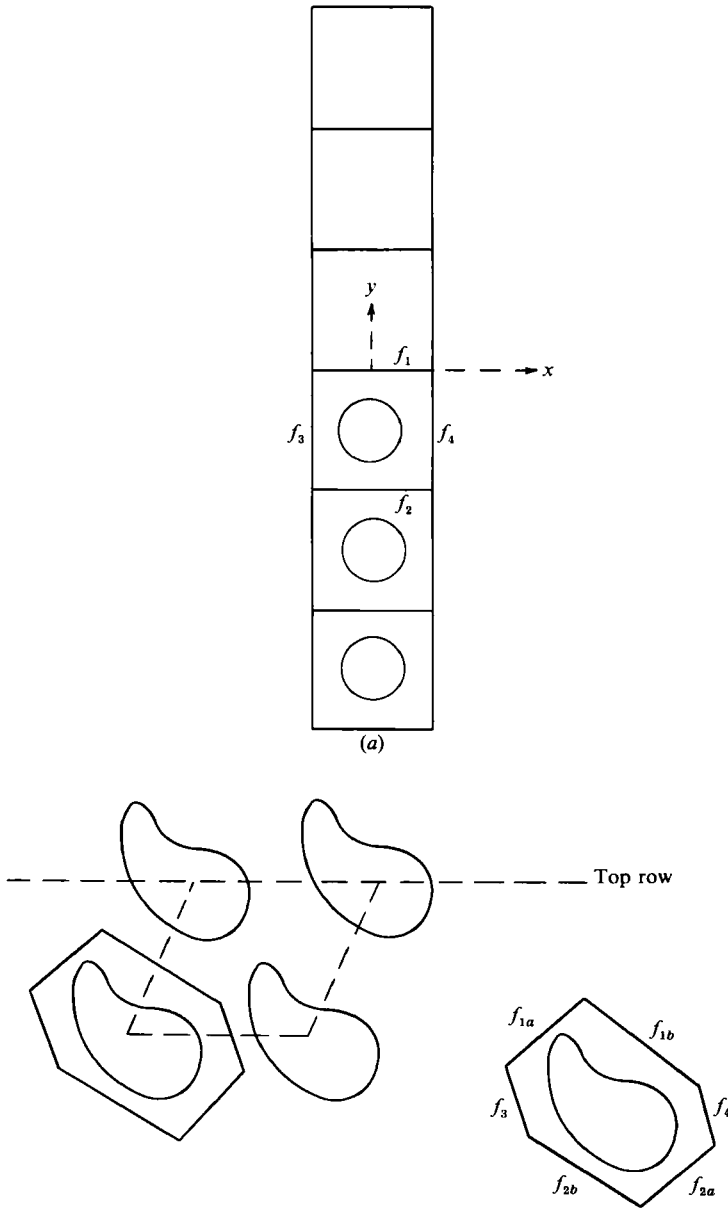
FIGURE 4. (a) Unit cells for a semi-infinite lattice of circular cylinders. (b) Unit cell for a general semi-infinite lattice.

We have periodic conditions at the sides of the cells

$$(u)_{f_3} = (u)_{f_4}, \quad \left(\frac{\mathrm{d}u}{\mathrm{d}n}\right)_{f_3} = -\left(\frac{\mathrm{d}u}{\mathrm{d}n}\right)_{f_4}, \tag{7}$$

and continuity conditions at the top and bottom of each cell

$$(u)^i_{f_1} = (u)^{i+1}_{f_2}, \quad \left(\frac{\mathrm{d}u}{\mathrm{d}n}\right)^i_{f_1} = -\left(\frac{\mathrm{d}u}{\mathrm{d}n}\right)^{i+1}_{f_2}, \tag{8}$$

where the superscript indicates the cell number, and the cells are numbered consecutively from bottom to top. At the top of the uppermost cell and the bottom of the lowermost cell we apply the infinity conditions

$$\left(\frac{\mathrm{d}u}{\mathrm{d}u}\right)_{y=+\infty} = \dot{\gamma}, \quad (u)_{y=-\infty} = 0. \tag{9}$$

The no-slip condition is simply $(u)_s = 0$ in each cell, since there is no pressure gradient and hence $u_p = 0$.

The simultaneous solution for the flow field in all cells would represent an extremely large and expensive computational effort. To avoid this problem we adopt an iterative method of solution. Consider the cell containing the top row of inclusions; let this be cell zero. In the first iteration we apply the infinity conditions at the top and bottom of this cell; that is $(\mathrm{d}u/\mathrm{d}n)^0 = \dot{\gamma}$ on f_1 and $(u)^0 = 0$ on f_2. With these specifications we calculate first approximations for u on the top and for $\mathrm{d}u/\mathrm{d}n$ on the bottom of this cell. These values give first approximations for the boundary conditions on the adjoining cells. Thus for the pure-fluid cell above we require

$$\left(\frac{\mathrm{d}u}{\mathrm{d}n}\right)^1_{f_1} = \dot{\gamma}, \quad (u)^1_{f_2} = (u)^0_{f_1}, \tag{10}$$

while for the lower cell with the inclusion

$$\left(\frac{\mathrm{d}u}{\mathrm{d}n}\right)^{-1}_{f_1} = -\left(\frac{\mathrm{d}u}{\mathrm{d}n}\right)^0_{f_2}, \quad (u)^{-1}_{f_2} = 0. \tag{11}$$

In each of these cells we calculate values for u at the top and $\mathrm{d}u/\mathrm{d}n$ at the bottom. These values are passed in turn to the next cells, and the process continues until the upper and lowermost cells are reached. To summarize, in each pure-fluid cell the boundary conditions are

$$\left(\frac{\mathrm{d}u}{\mathrm{d}n}\right)^1_{f_1} = \dot{\gamma}, \quad (u)^i_{f_2} = (u)^{i-1}_{f_1}, \tag{12}$$

while in each solid cell

$$\left(\frac{\mathrm{d}u}{\mathrm{d}n}\right)^i_{f_1} = -\left(\frac{\mathrm{d}u}{\mathrm{d}n}\right)^{i+1}_{f_2}, \quad (u)^i_{f_2} = 0. \tag{13}$$

At the start of the second iteration, we return to the zeroth cell. Now, instead of the infinity values, we employ the calculated values from adjoining cells in the previous iteration

$$\left(\frac{\mathrm{d}u}{\mathrm{d}n}\right)^0_{f_1} = -\left(\frac{\mathrm{d}u}{\mathrm{d}n}\right)^1_{f_2}, \quad (u)^0_{f_2} = (u)^{-1}_{f_1}. \tag{14}$$

This process is repeated for all cells. For the pure-fluid cells the boundary conditions are u on the bottom from the current iteration and $\mathrm{d}u/\mathrm{d}n$ on the top from the previous iteration. For the solid cells we use $\mathrm{d}u/\mathrm{d}n$ on the top from the current iteration and u on the bottom from the previous iteration. We continue in this way until we again reach the upper- and lowermost cells.

The third iteration follows in exactly the same manner, and the process continues. In practice, the corrections at each iteration overcompensate and the process as stated does not converge. This is easily corrected by introducing a relaxation parameter. Instead of simply replacing an old estimate by a new approximation, we employ a weighted average of the two. With this modification, the iteration converges rapidly.

The extension of this procedure for more general lattices is straightforward. Figure 3(b) shows a typical unit cell with the different sections of the cell perimeter labelled f_1-f_4. The periodicity boundary conditions are exactly as stated in (7). The matching conditions between adjoining cells and the steps in the iteration are also the same, the only differences being that f_1 and f_2 are slightly more general boundaries.

The method outlined above may be used to obtain accurate solutions for the shear flow over semi-infinite lattices; however, one additional modification may be introduced to improve the numerical results. In the pure-fluid cells, instead of solving for u directly, we solve for the disturbance velocity $u_d = u - \dot\gamma(y-y_0)$. With this definition, the calculated quantity tends to a constant at large y instead of a linear function of y. This minimizes the errors associated with the assumption of constant u on individual boundary elements.

A few words are appropriate concerning the computational effort required for the iterative procedure we have developed. In a typical problem we might have ten cells: five deep in the lattice and five above the lattice. If five iterations are needed for convergence, we must solve for the flow field in a typical cell on the order of 50 times. It would appear that a substantial increase in CPU time is needed compared with the infinite case. In actuality, very little additional computation is needed owing to the nature of the boundary-integral method. The major computation tasks are the calculation of the matrices A and B in (7) and the inversion of the resulting coefficient matrix in the system of equations for the unknown values of u and $\mathrm{d}u/\mathrm{d}n$. Once these calculations are completed, any number of boundary value problems for the same *cell geometry* may be solved with negligible effort. Since all pure-fluid cells and all solid cells are identical, the matrix calculations and inversion need be done only once for each type of cell. Further, the matrices for the pure-fluid cells are submatrices of those for the solid cells. In conclusion, the iterative solution for the semi-infinite problems requires computation time comparable to the solution for a single cell, with only slight increase as the number of cells or number of iterations is increased.

3. Axial flow through infinite arrays

In this section we apply the method described above to study pressure-driven flow in infinite arrays. We shall begin by considering a detailed description of the flow for a few simple arrays, and then show how the permeability is affected by the geometry of the array. To start, we examine the velocity profiles for square arrays of circular cylinders at three different concentrations. Figure 5(a) shows the profile for $c = 0.01$, characteristic of dilute arrays. In this case the velocity is nearly uniform over much of the interstitial area, with a logarithmic spike reducing U to zero on the small solid inclusions. This log r dependence is the asymptotic behaviour for all small inclusions independent of the lattice geometry or inclusion shape. Figures 5(b) and (c) show a smoother variation of velocity corresponding to concentrations $c = 0.1$ and 0.3 respectively. All curves have been drawn to the same scale, with velocities normalized with respect to GL_0^2/μ, where L_0 is the lattice spacing. Thus the vertical scale shows how the velocity decreases as the concentration is increased.

The shear stress on the surface of the solid inclusions is plotted in figure 6 as a function of angular position for four different concentrations. Each curve is normalized with respect to its average shear stress $GA_0/(2\pi a)$, where A_0 is the area of the unit cell. At small concentrations the stress is nearly uniform around the cylinder, while the variation is quite large for concentrations 0.7 and 0.785. This latter value is nearly equal to the close-packing limit $\frac{1}{4}\pi$. For high concentrations the extremely small gap
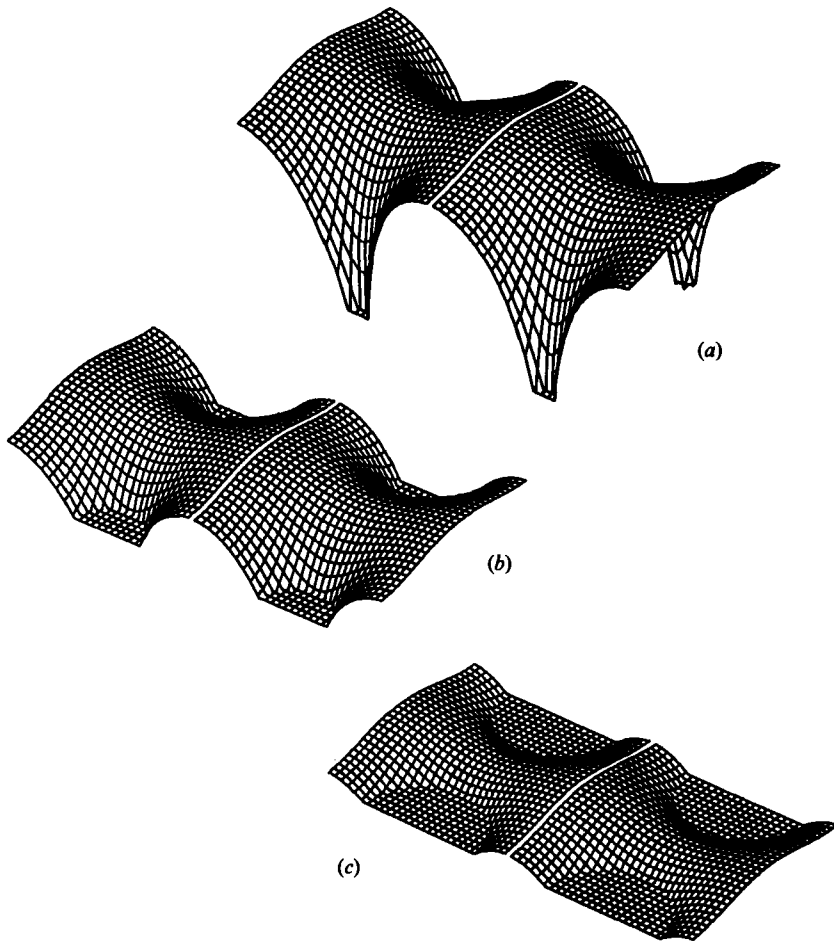
FIGURE 5. Perspective view of velocity profiles for pressure-driven flow through a square lattice of circular cylinders. Flat circular regions represent the area occupied by the cylinders; the vertical scale is proportional to velocity. Decreasing height from (a)-(c) reflects reduced flow as concentration (size of cylinders) is increased. (a) $c = 0.01$; (b) 0.1; (c) 0.3.

between cylinders allows negligible flow at the edges, and the shear stress drops to zero. The bulk of the flow is through the open channel centred among the cylinders. This is to be contrasted with transverse flow, for which the fluid would be forced through the gap.

A plot of shear-stress variation for hexagonal arrays of circular cylinders is shown in figure 7. The same qualitative behaviour is observed, with uniform stress at small concentrations and large changes at higher concentrations. Comparing the $c = 0.7$ curve with the same curve for the square lattice demonstrates that the hexagonal lattice will have more uniform stress distribution at any given concentration. This is simply because the hexagonal packing leads to a more uniform spacing between cylinders, with a larger cylinder gap at equal concentrations.

Next, we turn our attention to the permeability associated with the square and hexagonal lattices. The permeability K is defined in terms of the volume flow through the lattice, $K = \mu Q / G A_0$. Since K has units of length squared, we consider the dimensionless ratio K/A_0. The permeability for square and hexagonal lattices as a
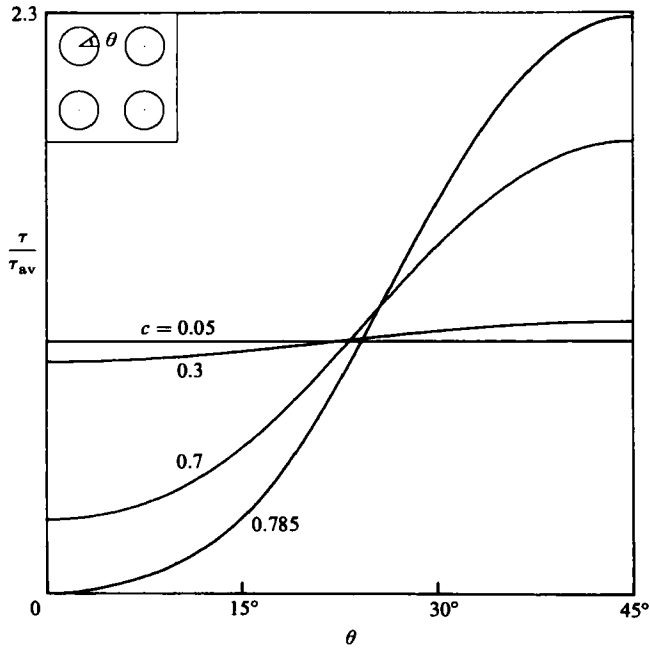
FIGURE 6. Shear stress as a function of angular position for a square lattice of circular cylinders.
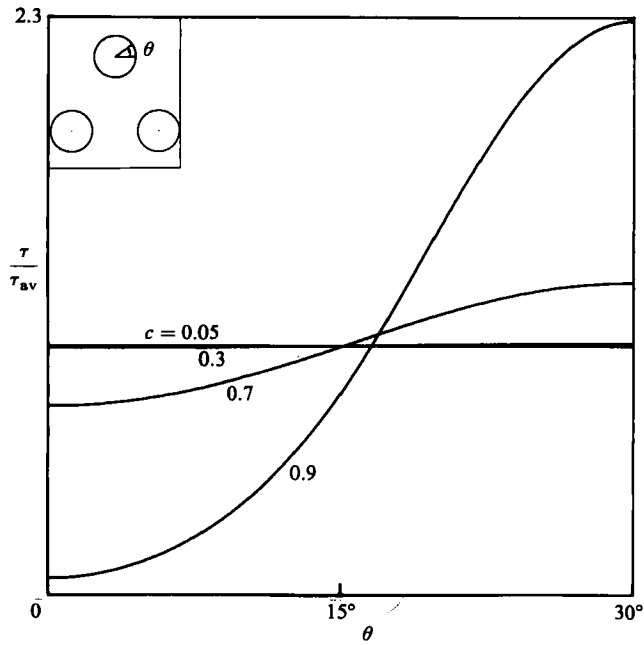
FIGURE 7. Shear stress as a function of angular position for a hexagonal lattice of circular cylinders.
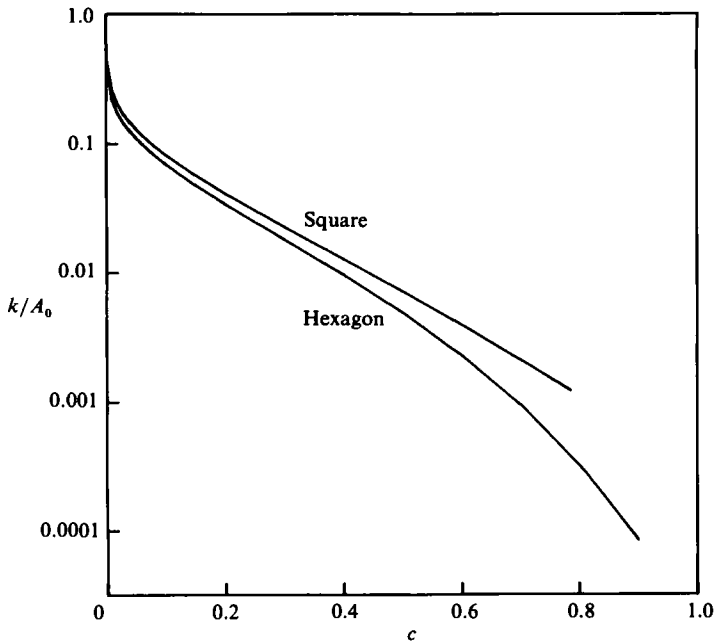
FIGURE 8. Permeability k/A_0 as a function of concentration for square and hexagonal lattices of cylinders.

function of concentration is shown in figure 8. The permeability for such lattices has been calculated previously by Sparrow & Loeffler (1959) using another method. Our results are in excellent agreement with these authors. Perhaps the most interesting result on this figure is that the square array has higher permeability for all values of concentration. This fact might have been predicted from our discussion above. The hexagonal packing has a more uniform gap between the cylinders, but this allows the square lattice a larger clear channel at the centre of each group of cylinders. Since volume flow rate increases rapidly with channel size (L^3 for flat plates, L^4 for cylinders), this clear channel gives a higher permeability for square lattices. As the concentration approaches zero, both lattices have the same asymptotic value $K/A_0 \sim (4\pi)^{-1} \ln c$, and the ratio of permeabilities approaches unity.

To further explore the effect of geometry on permeability, we consider more general inclusion shapes and lattice types. Consider a lattice of cylinder centres with base vectors $(L_0, 0)$ and $(H \cos \theta, H)$. A unit cell in this lattice is a parallelogram with base L_0, height H_0 and interior angle θ. Centred on the vertices of this parallelogram, the cylinder cross-sections are chosen to be ellipses of aspect ratio a/b, with the major axis tilted at an angle ϕ with respect to the x-axis. The family of arrays thus constructed is characterized by five parameters $(H_0/L_0, \theta, a/b, \phi, c)$.

First, let us consider the effect of the lattice angle θ. With $L_0 = H_0$ and $a/b = 1$, the array of circular cylinders changes from a square lattice to a staggered lattice as θ varies from $90°$ to $63.43°$. At this angle, each cylinder is centred between the pair in adjoining rows. (Note that a hexagonal array is not included in this family, because it has $H_0/L_0 = \frac{1}{2}\sqrt{3}$.) The permeability for these arrays as a function of θ is shown in figure 9, normalized with respect to the value for a square array. At low concentrations, the permeability is nearly independent of the stagger angle. At high concentrations the permeability varies dramatically, with the value for maximum
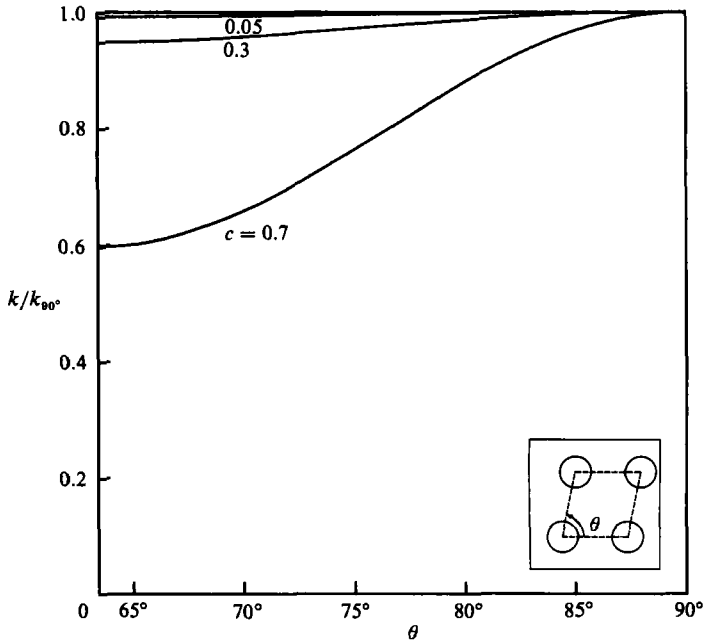
FIGURE 9. Permeability as a function of lattice angle for arrays of circular cylinders.
Permeability is normalized with respect to its value for $\theta = 90°$.

stagger dropping to 60 % of that for a square lattice. This behaviour is analogous to that observed for hexagonal arrays. In each case the staggered array leads to a more uniform cylinder spacing, more uniform stress distribution and lower flow rate.

As the next array parameter, we take the aspect ratio of the inclusions a/b. Several families of arrays are shown in figure 10, with aspect ratios varying from 1 to as high as 10. For each family the permeability is normalized with respect to the member of that family with $a/b = 1$. The three arrays at high concentration (10 a–c), $c = 0.3$, show dramatically different behaviour, which can be explained by a simple geometric principle. For the square lattice with $\phi = 0$, increasing a/b increases the size of the clear channel. As with the previous arrays, for inclusions of comparable wetted surface, the size of the clear channel is the most important factor for determining the permeability. At small concentrations (figure 10d–f) each geometry approaches an array of flat plates, and the permeability dependence is similar in all cases. The ratio K/K_0 would be even larger for still lower concentrations, since an array of flat plates with zero volume fraction has finite permeability, while the permeability for arrays of cylinders becomes infinite $\sim \ln c$.

The final set of infinite arrays to be considered consists of elliptical cylinders with varying tilt angle ϕ. The permeability is plotted in figure 11 normalized with respect to its value at $\phi = 0$. In each case the aspect ratio is $a/b = 2$. At small concentration $c = 0.05$ a square lattice shows little variation as a function of ϕ. This is to be expected since the inclusions are fairly small and interactions are not important. For larger concentration, $c = 0.3$, both the square and hexagonal lattices show moderate fluctuation. The hexagonal array shows less variation because its inclusions are farther apart. Each array shows a permeability minimum at its maximum tilt angle owing to the reduction in size of the large clear channel.
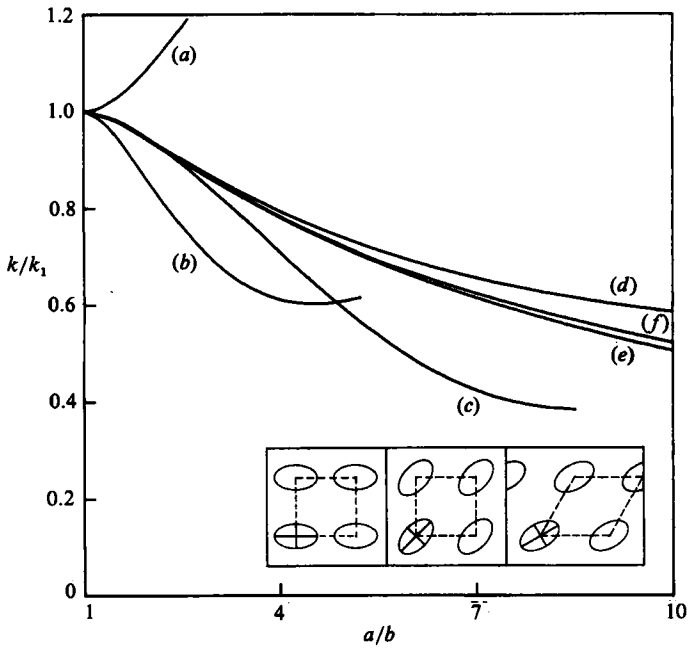
FIGURE 10. Permeability versus aspect ratio of elliptical inclusions for several lattice types; permeability is normalized with respect to its value at $a/b = 1$: (a) square lattice, $\phi = 0°$, $c = 0.3$; (b) square lattice, 45°, 0.3; (c) hexagonal lattice, 30°, 0.3; (d) square lattice, 0°, 0.05; (e) square lattice, 45°, 0.05; (f) hexagonal lattice, 30°, 0.05.
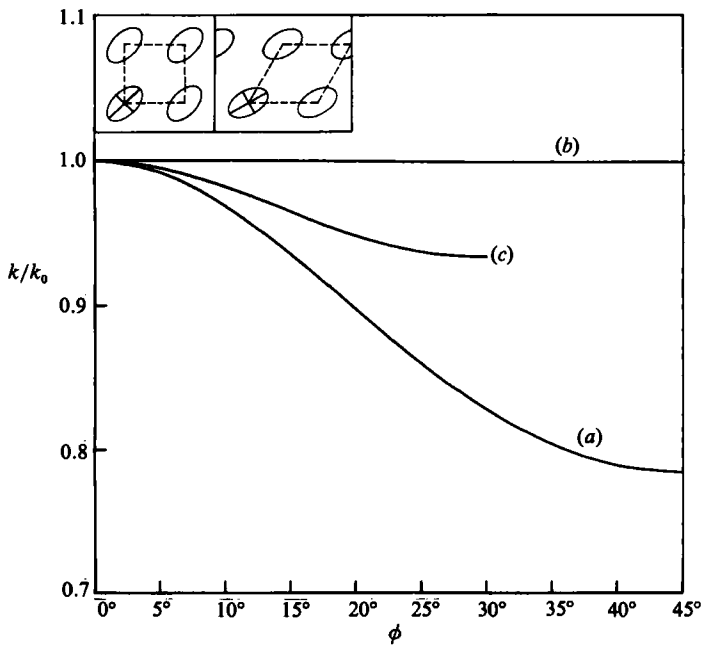
FIGURE 11. Permeability as a function of inclusion axis tilt angle ϕ for elliptic cylinders of aspect ratio 2:1, normalized with respect to the value for $\phi = 0°$; (a) square lattice, $c = 0.3$; (b) square lattice, 0.05; (c) hexagonal lattice, 0.3.

4. Axial flow in semi-infinite arrays

The primary goal of this paper is to investigate the flow near the surface of porous media. We address this issue by considering flow through semi-infinite lattices with a simple shear flow in the pure fluid above the lattice. Velocity profiles in the first two cells of such a lattice are shown schematically in figure 12. A more precise plot of the velocity profile for square lattices of circular cylinders is given in figures 13 (a–c) for three different concentrations: $c = 0.05, 0.001, 0.00001$. In each case the dashed lines and solid lines represent velocity profiles at the positions sketched in figure 12. The most striking feature of these plots is how quickly the velocity develops a self-similar profile, which is repeated as we go deeper into the lattice. From the very first cell $(0 < y < 1)$, which extends above the first row of inclusions, the velocity along the centreline plane (solid line) is nearly unchanged except for the scaling factor in each cell. In the plane intersecting the inclusions (dashed line), the first cell shows a simple shear profile, while all cells beneath this cell have similar profiles. The rapid development of the self-similar profiles is especially surprising given the low concentration of these arrays. The effects of concentration on the velocity are readily apparent in figure 13. First, the highest concentration $c = 0.05$ causes a much more rapid decrease in velocity than for the other arrays. Secondly, we observe a significant difference between the velocity profiles in the centreline plane and in the inclusion plane for the high-concentration array. As the concentration decreases, these curves more closely approach each other. For asymptotically small concentrations, the two profiles will coincide except for a sharp spike reducing the velocity to zero on the inclusions. This spike is of the form $\ln r$ because its asymptotic effect is that of an axial point force. Velocity profiles for high concentrations will resemble figure 13 (a) with a more rapid decay in the velocity and smaller flow in the inclusion plane.

The shear-stress distributions for the three arrays considered above are plotted in figures 14 (a–c). Only the stress in the first two rows of the lattice is shown. The rapid drop off in shear stress from the top row to the second row clearly demonstrates the decay of the velocity field in the lattice. The distribution of shear stress around the cylinder (figure 14 a) also reflects this behaviour, with its value at the bottom $(\theta = -90°)$ being a small fraction of its value at the top of the cylinder $(\theta = 90°)$. As with the infinite arrays, the stress distribution becomes more uniform as the concentration decreases.

4.1. Slip velocities for simple arrays

One way to interpret the surface flow in a macroscopic sense is to define a slip velocity as discussed in §1. Let us define the nominal interface of the medium to be the plane intersecting the inclusion centres in the top row of the lattice. The slip velocity for a simple shear flow over the medium is just

$$u_s = \frac{k^{\frac{1}{2}}}{\alpha}\dot{\gamma} + O(k). \tag{15}$$

To illustrate the sensitivity of this condition to the choice of the interface plane, consider a vertical shift of the nominal interface of magnitude δ. This induces a change in the slip velocity of order $\dot{\gamma}\delta$. If δ is only as large as the cylinder radius a, the change in u_s is $\dot{\gamma}a$, which is much larger than the leading term if $a \gg k^{\frac{1}{2}}$, or equivalently if $c \gg k/A_0$. This condition holds for all geometries considered in figure 8, except for those of very small concentration $c < 0.02$. We conclude that the slip velocity is likely to be extremely sensitive to the position of the interface.
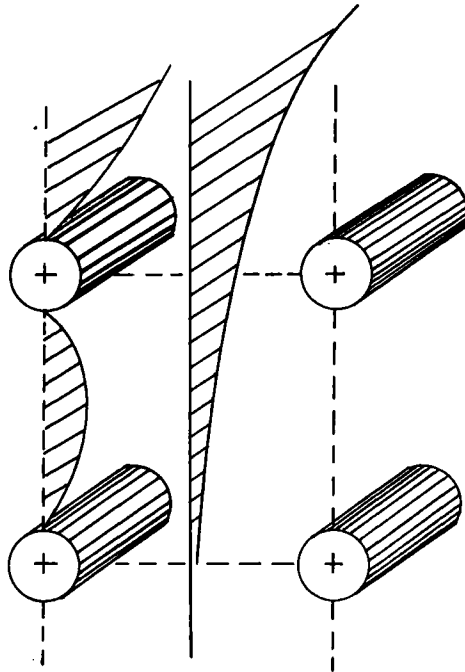
FIGURE 12. Schematic view of velocity profiles in a semi-infinite lattice of cylinders.

To calculate a slip velocity, we calculate the total volume flux Q^+ between the interface and a plane a distance h above the interface

$$Q^+ = \int_0^{L_0} \int_0^h u\, dy\, dx. \tag{16}$$

Equating this flux with the macroscopic prediction

$$Q^+ = u_{\rm s} h + \tfrac{1}{2}\gamma h^2 \tag{17}$$

gives the value of the slip velocity. This is equivalent to the experimental procedure of Beavers & Joseph. Note that the prediction for $u_{\rm s}$ is insensitive to h for all values greater than approximately one cell height.

Another way to define the slip velocity is in terms of the volume flow rate below the interface. If we assume the flow on a macroscopic level is described by Brinkman's equation with $\mu^* = \mu$ then the mean velocity is given by

$$u = u_{\rm s}\, e^{y/k^{\frac{1}{2}}}, \tag{18}$$

and the flux between the interface and a plane at $y = -h$ is

$$Q^- = u_{\rm s}\, k^{\frac{1}{2}}(1 - e^{-h/k^{\frac{1}{2}}}). \tag{19}$$

Equating this expression with the calculated value for Q^- gives the value of the slip velocity.

Values of the slip velocity based on the flux above and below the interface are shown in figure 15 for square and hexagonal lattices of circular cylinders. The dashed curve is based on the flux above the interface, while the solid curve is based on the flux below. We see a noticeable disparity between the two definitions except at exceedingly small concentrations. The traditional definition based on the flux above
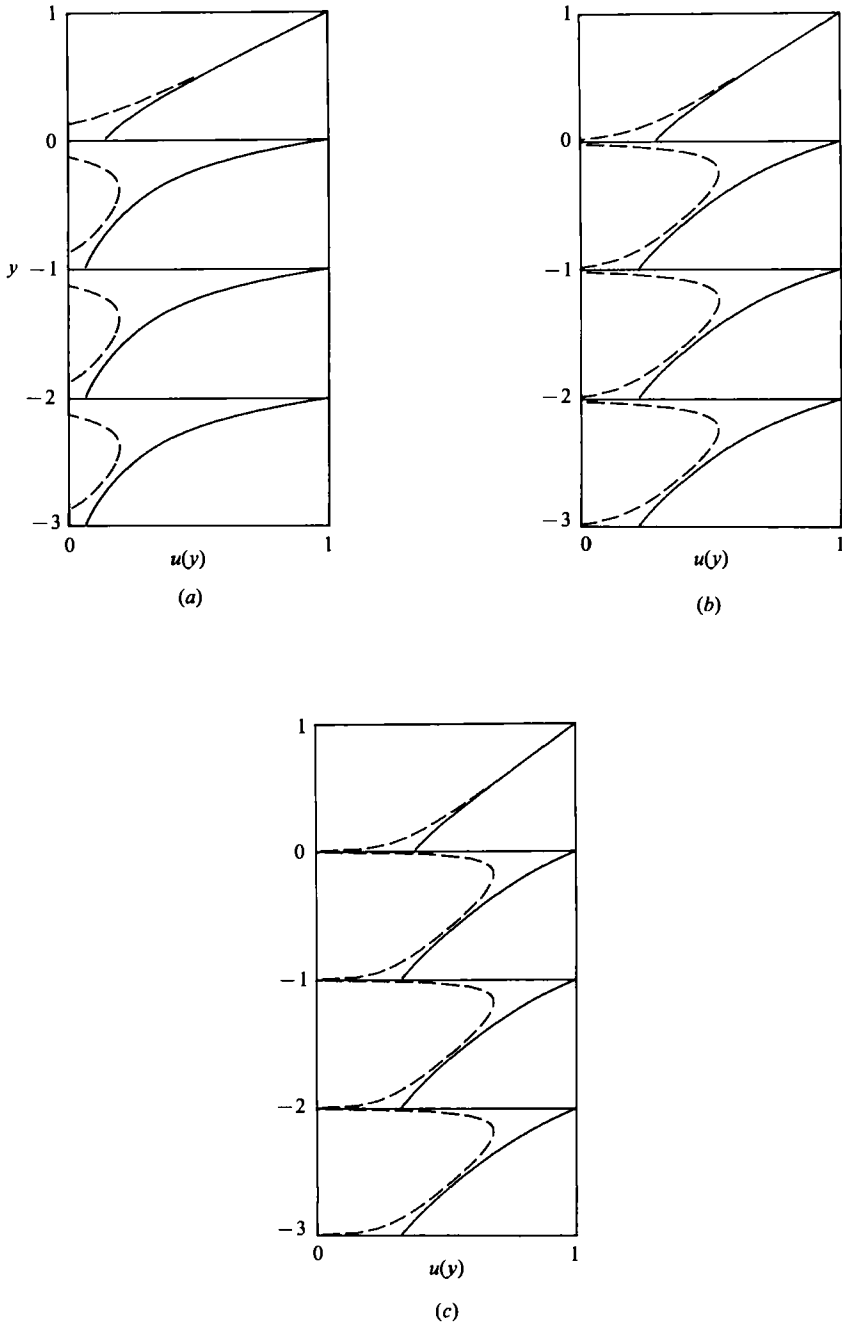
FIGURE 13. Velocity profiles for square lattices of circular cylinders. Dashed and solid lines correspond to positions illustrated in figure 12. The velocity in each vertical panel is scaled to show self-similar profiles. (a) $c = 0.05$, scaling factors for velocity 0.990, 7.16, 116, 1890. (b) $c = 0.001$, scaling factors for velocity 0.786, 2.78, 12.8, 59.4. (c) $= 0.00001$, scaling factors for velocity 0.675, 1.80, 5.51, 16.9.
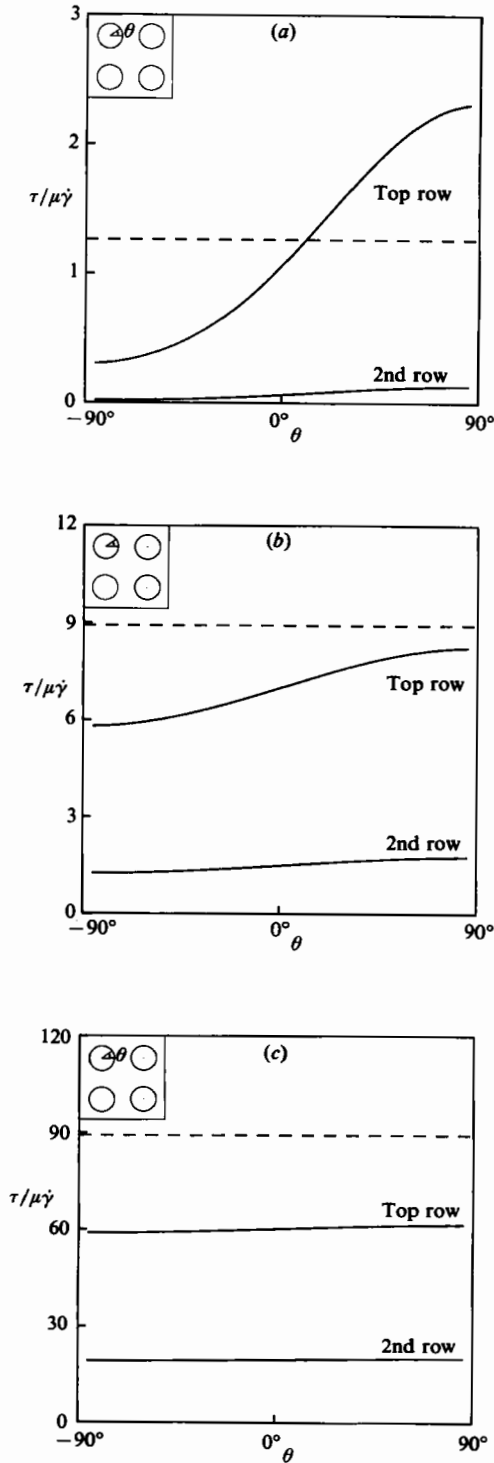
FIGURE 14. Shear stress as a function of angular position for semi-infinite lattices of circular cylinders: (a) $c = 0.05$; (b) 0.001; (c) 0.00001.

the interface may even take on negative values owing to the slight protrusion of the inclusions above the nominal interface. If the interface were chosen as the plane tangent to the top row of cylinders, the slip velocity would be shifted upward and would be positive for all concentrations. Since such a change would be indiscernible on a macroscopic level, we conclude that it is not possible to define a consistent value for the slip velocity. All reasonable choices for α are equivalent subject to microscopic changes in the definition of the interface.

4.2. *Decay factor*

Another important characteristic of flow near the surface of a porous medium is the rate at which the velocity decays as we enter the medium. Brinkman's equation predicts

$$u = u_s \exp\left[y/k^{\frac{1}{2}}\left(\frac{\mu^*}{\mu}\right)^{\frac{1}{2}}\right], \tag{20}$$

which describes the decay of the macroscopic average velocity.

An estimate for the quantity $(\mu^*/\mu)^{\frac{1}{2}}$ may be obtained by calculating the decay ratio of the velocity between two points in the medium

$$d = \frac{u(y+\Delta y)}{u(y)} = \exp\left[\Delta y/k^{\frac{1}{2}}\left(\frac{\mu^*}{\mu}\right)^{\frac{1}{2}}\right], \tag{21}$$

From which we have

$$\left(\frac{\mu^*}{\mu}\right)^{\frac{1}{2}} = \frac{\Delta y}{k^{\frac{1}{2}}\log d}. \tag{22}$$

Since the microscopic velocity varies over each cell, we calculate $(\mu^*/\mu)^{\frac{1}{2}}$ from the average velocity in two adjoining cells. Owing to the rapid development of the self-similar flow fields, this value is insensitive to the cells chosen, for all cells below the first.

The effective value of $(\mu^*/\mu)^{\frac{1}{2}}$ for simple arrays of circular cylinders is shown in figure 16 as a function of concentration. Above a concentration of $c = 0.4$ the velocity decays so rapidly over each cell that it is not meaningful to define a decay ratio in analogy with Brinkman's equation. Over the range of concentrations presented, $(\mu^*/\mu)^{\frac{1}{2}}$ remains close to 1, implying that Brinkman's equation provides a reasonable description of the rate of decay of the flow field.

To further analyse the effect of geometry on decay rate, we consider lattices of more general configuration. The decay factor $(\mu^*/\mu)^{\frac{1}{2}}$ for staggered lattices with $L_0 = H_0$ and θ running from 90° to 63.43° is plotted in figure 17. This curve shows the decay factor to be nearly independent of lattice stagger.

The effect of the inclusions' aspect ratio for four different arrays is shown in figure 18. The most interesting curves in this figure are those corresponding to the square arrays $\phi = 0°$ and $\phi = 90°$. For infinite media these two arrays are identical, being distinguished only by a 90° rotation of the array. Thus they might represent two different 'slices' of the same material. As the aspect ratio a/b approaches infinity, array 18(a) approaches a set of flat plates normal to the interface, while 18(b) approaches a set of plates parallel to the interface. In both cases, the permeability approaches a finite value, but the decay factor for 18(a) is finite, while that for 18(b) approaches zero as the flat plates shut off the flow in the interior. In this example it is clear that we have an anisotropic medium for which the decay rate is anisotropic
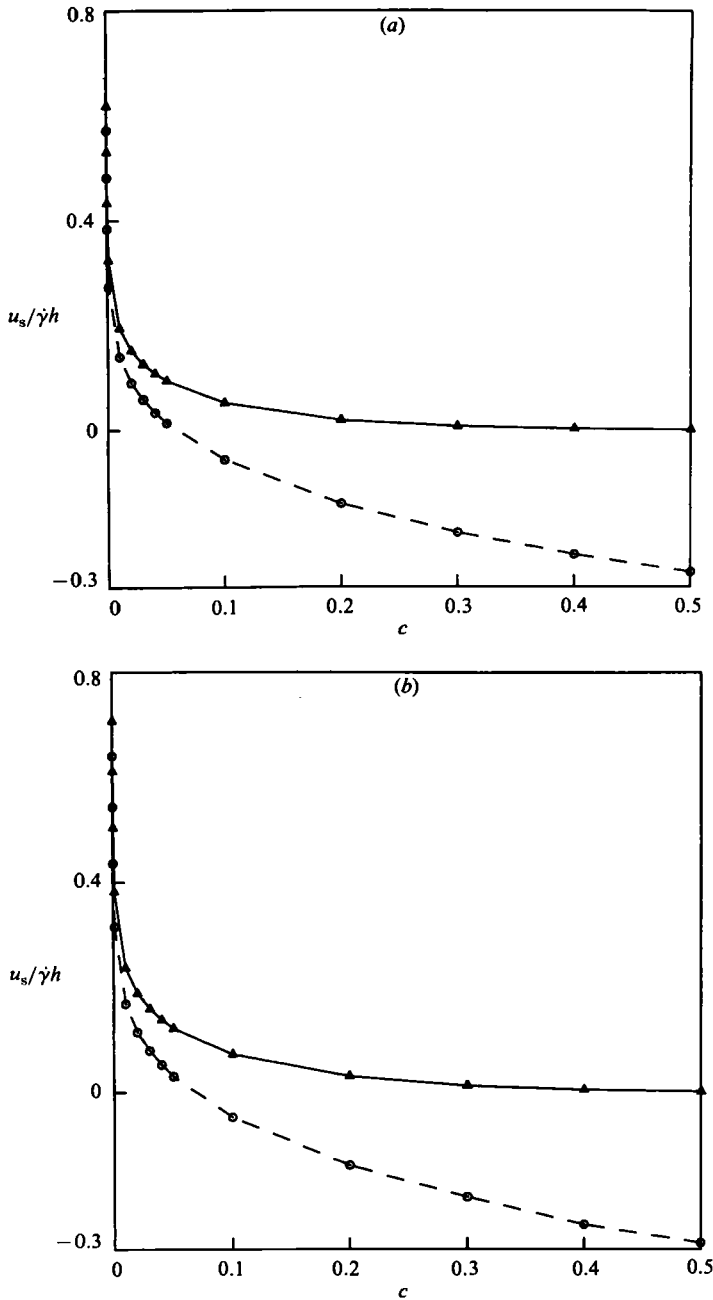
FIGURE 15. Slip velocity as a function of concentration for (*a*) a square lattice, (*b*) a hexagonal lattice. Solid line is based on flow rate below interface. Dashed line is based on flow above interface.

as well as the permeability tensor. The decay rate is affected by the permeability in the flow direction and by some measure of flow resistance in the direction normal to the surface. This resistance may be related to the permeability for flow normal to the surface, but is not necessarily expressible as a function of permeability alone.

Unfortunately, Brinkman's equation is unable to distinguish between the two media in this example, even with the introduction of an anisotropic permeability
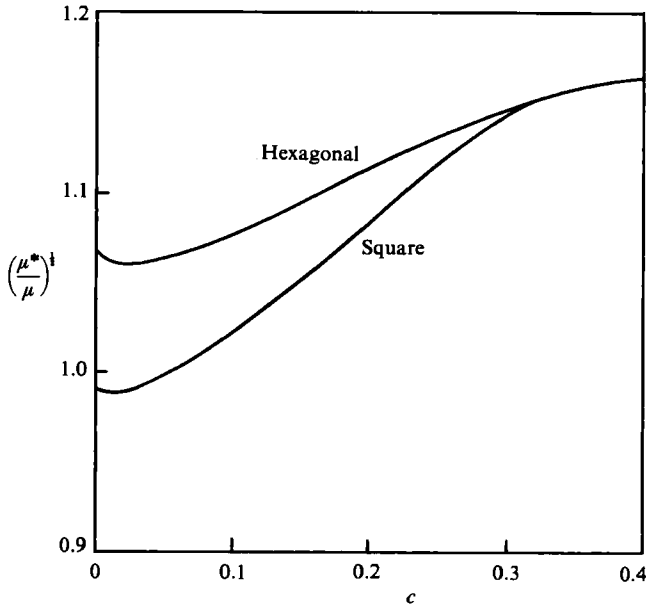
FIGURE 16. Decay factor $(\mu^*/\mu)^{\frac{1}{2}}$ as a function of concentration for square and hexagonal arrays of circular cylinders.
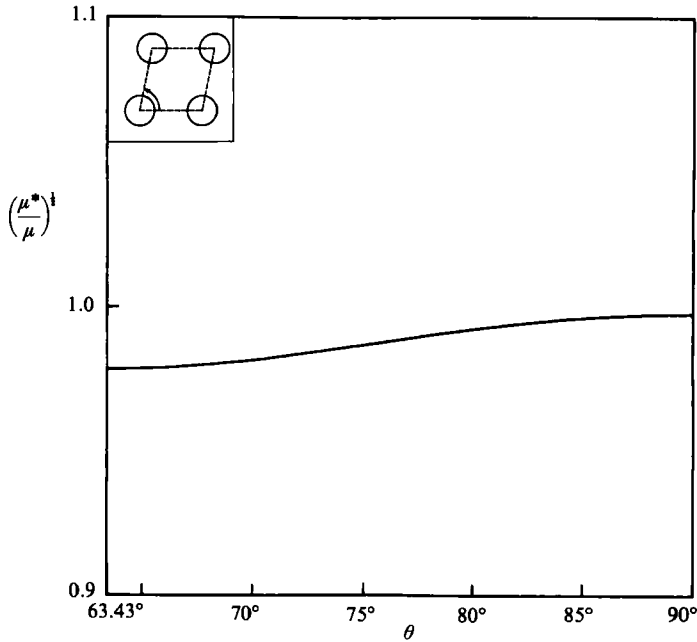
FIGURE 17. Decay factor $(\mu^*/\mu)^{\frac{1}{2}}$ as a function of lattice angle θ for circular cylinders, $c = 0.05$.
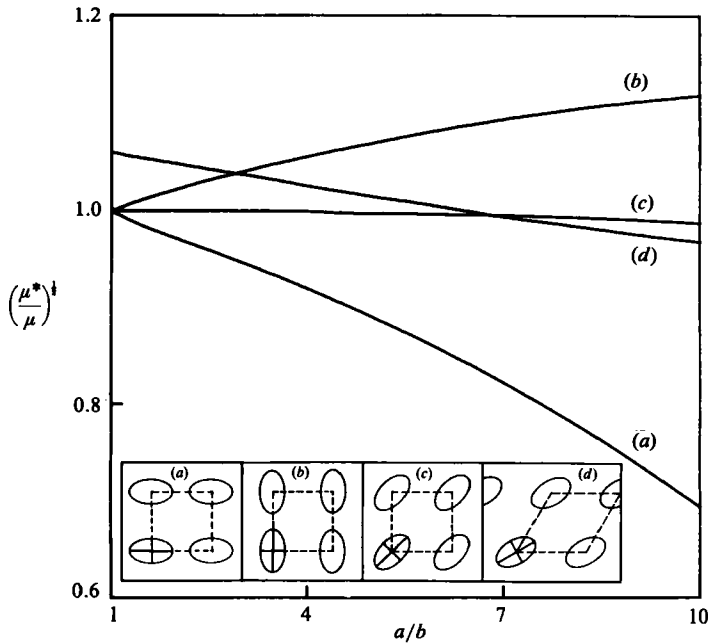
FIGURE 18. Decay factor $(\mu^*/\mu)^{\frac{1}{2}}$ as a function of inclusion aspect ratio for different lattice types: (a) square, $\phi = 0°$; (b) square, $90°$; (c) square, $45°$; (d) hexagonal, $30°$.

tensor. The coordinate system with flow along the z-axis and interface in the plane $y = 0$ coincides with the principal axes of the permeability tensor. Thus the permeability is diagonal and only the k_{33} component enters Brinkman's equation for the axial flow. We conclude that Brinkman's equation gives identical predictions for the two vastly different flows in the example given above. The only resolution for such problems is to adopt a more rigorous model of porous media, including terms such as those proportional to the velocity gradient, in the form $M_{ijk}\, \partial u_j/\partial x_k$.

In summary, we find that Brinkman's equation may be worthwhile for describing axial flow through lattices isotropic in the plane normal to the flow. For more general media, it may fail to predict the flow field even in a qualitative sense. It is not possible to define a consistent value for slip coefficients for *any* media, because microscopic changes in the position of the nominal interface lead to $O(1)$ changes in the slip coefficient. Thus all reasonable choices for α are equivalent, being distinguished by translations of the nominal interface which are indiscernible on a macroscopic level.

REFERENCES

BEAVERS, G. S. & JOSEPH, D. D. 1967 Boundary condition at a naturally permeable wall. *J. Fluid Mech.* **30**, 197–207.

BEAVERS, G. S., SPARROW, E. M. & MASHA, B. A. 1974 Boundary condition at a porous surface which bounds a fluid flow. *AIChE J.* **20**, 596–597.

BREBBIA, C. A. (ed.) 1983 *Boundary Element Techniques in Computer-Aided Engineering*. Martinus Nijhoff.

BRINKMAN, H. C. 1947 A calculation of the viscous force exerted by a flowing fluid on a dense swarm of particles. *App. Sci. Res.* **A1**, 27.

DARCY, H. P. G. 1856 *Les Fontaines Publiques de la Ville de Dijon*. Paris: Victor Dalmont.

HOWELLS, I. D. 1974 Drag due to the motion of a Newtonian fluid through a sparse random array of small rigid fixed objects. *J. Fluid Mech.* **64**, 449–475.

MATSUMOTO, K. & SUGANUMA, A. 1977 Settling velocity of a permeable model floc. *Chem. Engng Sci.* **32**, 445–447.

RICHARDSON, S. 1971 A model for the boundary condition of a porous material. Part 2. *J. Fluid Mech.* **49**, 327–336.

SAFFMAN, P. G. 1971 On the boundary condition at the surface of a porous medium. *Stud. Appl. Maths* **50**, 93–101.

SANGANI, A. S. & ACRIVOS, A. 1982a Slow flow past periodic arrays of cylinders with application to heat transfer. *Intl J. Multiphase Flow* **8**, 193–206.

SANGANI, A. S. & ACRIVOS, A. 1982b Slow flow through a periodic array of spheres. *Intl J. Multiphase Flow* **8**, 343–360.

SNEDDON, I. N. 1957 *Elements of Partial Differential Equations*. McGraw-Hill.

SPARROW, E. M. & LOEFFLER, A. L. 1959 Longitudinal laminar flow between cylinders arranged in a regular array. *AIChE J.* **5**, 325–330.

TAYLOR, G. I. 1971 A model for the boundary condition of a porous material. Part 1. *J. Fluid Mech.* **49**, 319–326.

ZICK, A. A. & HOMSY, G. M. 1982 Stokes flow through periodic arrays of spheres. *J. Fluid Mech.* **115**, 13–26.